On the L-PBF Fabrication of a Novel Medium Carbon, High Silicon Nanostructured Bainitic Steel with and Without Substrate Pre-heating: Density and Microstructural Investigation

MATTIA FRANCESCHI ,[1,5] ENRICO SAGGIONETTO,[2] ARSHAD YAZDANPANAH,[3]
LUCA PEZZATO,[4] ANNE MERTENS,[2] and MANUELE DABALA`[3]

1.—Department of Engineering and Management, University of Padova, 36100 Vicenza, Italy. 2.—Metallic Materials for Additive Manufacturing (MMS), A&M Department, University ofLiege, 4000 Liege, Belgium. 3.—Department of Industrial Engineering, University of Padova, Via Marzolo 9, 35131 Padua, Italy. 4.—Institute of Condensed Matter Chemistry andEnergy Technologies (ICMATE) National Research Council of ItalyC.so Stati Uniti 4, 35127 Padua, Italy. 5.—e-mail: franceschimattia@gmail.com

Laser powder bed fusion (L-PBF) metals are often characterized by fabrication defects, such as lack of fusion and stress-induced cracks, which significantly impact the mechanical behavior and structural integrity of the produced components. Substrate pre-heating has emerged as an effective strategy to enhance part density and reduce defect formation. During the fabrication of advanced high-strength steels (AHSS), the combination of high hardenability and rapid cooling rates typically results in untempered martensitic microstructures, necessitating post-fabrication heat treatments, increasing the manufacturing process's complexity, duration, and cost. In this study, the effects of substrate pre-heating and in situ heat treatment were investigated using a nanostructured bainitic steel with a composition of 0.38C-3.2Si-2.8Mn0.1Al (wt.%). Substrate pre-heating at 320C, combined with a 1.5-h isothermal holding following fabrication, resulted in improved specimen density and a significant reduction in process-induced cracks. Furthermore, an in situ isothermal heat treatment during fabrication facilitated the development of the desired nanostructured-bainitic microstructure, eliminating additional post-fabrication heat treatments. A comprehensive specimen characterization was conducted using optical microscopy (OM), SEM, TEM, XRD, and nanohardness measurements. The results demonstrate the potential of combining substrate pre-heating with in situ heat treatment to optimize the microstructure of AHSS fabricated via L-PBF while streamlining the manufacturing process.

INTRODUCTION

Over the last 2 decades, additive manufacturing (AM) has been subjected to intensive research in both industry and academia.[1] One of the primary drivers of this growing interest is its broad applicability to virtually all classes of materials,[2] ranging from metals to ceramic materials. AM offers flexibility, scalability, and the capability to produce structural components, with unlimited complex geometries and intricate features, which are hardly achieved with the conventional methods, such as forging, casting, and subtractive technologies (machining, etc.).[1,3] In addition to these advantages, AM enables efficient use of raw materials, significantly reducing waste and lowering production costs. Furthermore, it aligns well with the increasing demand for customized parts for niche applications and meets the requirements imposed by novel business models, which prioritize reduced time to market. As a result, research efforts have inevitably shifted toward the development of additive manufacturing processes.[2]

In the context of metallic materials, several AM technologies have been developed in recent years, including (1) powder bed systems, (2) powder feed systems, and (3) wire feed systems and binder jetting systems.[4] Currently, the most widely adopted AM method for metals, particularly within the powder bed systems, is the selective laser melting (SLM) process, also called the laser powder bed fusion (L-PBF) process.[4] In L-PBF, successive layers of metal powder are selectively melted one above another using a high-power laser, which entails the asynchronous layer-by-layer construction of 3D fully dense near-net-shape components directly from a computer-aided design CAD model.[1,5] The process involves powder deposition onto a substrate or a previously deposited layer, followed by selective melting according to the component geometry.[1] After each layer has been processed, the build platform is lowered to allow for the subsequent recoating step.

Numerous studies have shown that L-PBF is among the most promising techniques, as the process enables the production of metallic parts with mechanical properties comparable to those of conventionally fabricated parts. Nonetheless, some challenges and defects—such as porosities, cracking, undesired phase formation, and residual stresses—currently limit its widespread industrial application.[6] L-PBF has been successfully employed for various metallic alloys, including, but not limited to, Al-alloys such as Al-Si[7] and Al-Si-Mg alloys,[5,8] copper and CuCrZr alloys,[9,10] Ti alloys,[11] nickel-based superalloys,[12–14] refractory metals,[15,16] and steels.[17–21] In particular, there is a growing interest in using different steel grades for part fabrication via SLM, including stainless steels,[22] hot work tool steels,[23] and precipitation-hardening[23] and maraging[23] steels to produce structural parts with high performance (mechanical and corrosion). However, there is still limited interest in manufacturing advanced high-strength steels.

Over the past 2 decades, three generations of advanced high-strength steels (AHSS) have been developed with the dual objective of reducing CO_2 emissions—thus aligning with European Union environmental regulations—and enhancing the safety and durability of structural components.[24,25] The first generation of AHSS includes dual-phase (DP), complex phase (CP), and transformation-induced plasticity (TRIP) steels. These steel grades were conceptualized with relatively lean compositions and ferritic-based multi-phase microstructures, with improved formability, strength, and elongation phenomena of strain-induced transformation.[26] Despite significant improvements over existing high-strength steels, limitations in formability and weldability persist.

The second-generation AHSS undeniably showcases superior mechanical properties. and comprises heavily alloyed austenitic steels (Mn > 15%wt.%). Among these, there are twinning-induced plasticity (TWIP) steels,[27] lightweight steels with induced plasticity (L-IP), and shear band strengthened steels (SIP).[28,29] Although these steels offer exceptional mechanical performances (UTS 9 Total Elongation ‡ 50 GPa%) primarily due to the mechanical twinning (TWIP effect) in high-manganese steels, their adoption is limited. This is attributed to challenges including poor castability, restricted hot workability, reduced corrosion resistance, and high production costs related to their elevated manganese content.[30]

Finally, the third generation, currently under development, includes multiphase steels (medium manganese steels,[31] Q&P[32]). These materials aim to combine the benefits of the previous generations while improving processability and limited costs.[30,33,34] Among these, steels featuring a nanostructured, carbide-free bainitic microstructure have gained significant interest because of their remarkable balance of strength and ductility, often achieving UTS values > 1.5 GPa and elongations around 20%. The development of these steels is rooted in the pioneering work of Bhadeshia and Edmonds,[35] with an substantial contribution from Caballero and Garcia-Mateo,[36–38] who formulated the modern theory of bainite transformation and provided a fundamental framework for alloy design. These steels exhibit unique mechanical properties, and a microstructure consisting of nanoscale bainitic ferrite and carbon-enriched austenite,[39] representing the first-generation bulk nanostructured steel, without adopting severe plastic deformation (SPD) approaches, such as equal-channel angular extrusion (ECAP), accumulative roll bonding (ARB), and high-pressure torsion (HPT), was obtained.

According to the bainite transformation theory, bainitic ferrite forms through the decomposition of austenite during isothermal treatments at temperatures below those for pearlite formation but above the martensite start temperature. The resulting ferrite appears in sheaf-like structures composed of subunits sharing a common crystallographic orientation.[40] Its formation includes a para-equilibrium nucleation, where only carbon partitions, and by a displacive diffusionless growth, where there is no change in the chemical composition between the parent and the child phase.[40] Carbon partitioning from bainitic ferrite to the untransformed austenite enhances thermal and mechanical stability, promoting substantial retention of austenite at room temperature.

The retained carbon-enriched austenite exhibits a twofold morphology: (1) film-like, with high carbon content and located between the subunits of bainitic ferrite; (2) blocks located between the various sheaves, having a lower carbon content compared to the films, resulting in lower mechanical and thermal stability.[41–43] Both microstructural constituents play a pivotal role in determining the mechanical performance. The nanoscale bainitic ferrite (thickness< 100 nm) contributes mainly to the strength, aided by the solid solution strengthening given by the alloying elements. On the other hand, retained austenite enhances the ductility of such steels through the strain-induced martensitic transformation under loads and the twins present in the austenite films.[44]

The typical composition of these steel grades falls within the following ranges: (0.4–1)C-(‡ 1.5)Si-(0.7– 2)Mn-(0.4–1.7)Cr-(0–0.2)Mo wt.%.[39] Medium-tohigh carbon contents are required to obtain low martensite start temperatures and nanosized microstructural constituents. The addition of silicon (‡ 1.5 wt.%) and aluminum effectively suppresses cementite precipitation during isothermal holding treatments, as both are not soluble in cementite. This promotes the stabilization of highly carbonenriched austenite at room temperature. The high carbon in solid solution facilitates a reduction in the initiation temperature of martensitic transformation below room temperature, preventing any other phase transformation after the final cooling stage. Furthermore, a significant contribution to microstructural refinement is given by silicon, which leads to obtaining bainitic ferrite plates with a thickness in the order of tens of nanometers.

Manganese and other elements are fundamental in controlling hardenability, which is generally high enough to eliminate the need for rapid quenching during austempering.[40]

Investigating the applicability of AHSS to AM is important as it aligns with the European Green Deal and the broader pursuit of high-performance, lightweight components, particularly in the automotive sector, where crashworthiness is a key consideration. To date, indeed, the literature reports only a limited number of studies dedicated to medium- to high-manganese steels, which have yielded promising results, or to quench and tempered steels (Q&T).[45] However, to date, no in-depth research has been conducted regarding carbide-free bainitic steels, except for a preliminary work conducted by the same authors on steel with a medium carbon an silicon content.[46,47] This preliminary study highlighted the possibility of obtaining components with high relative density but with numerous internal and surface imperfections (lack of fusion, cracks, etc.). Due to the high cooling rates associated with the L-PBF process, the final microstructure was found to be martensitic rather than the expected one. Therefore, this study aims to optimize processing parameters to improve part integrity, minimize the defect content, and tailor the microstructure. These goals were pursued through substrate preheating, a strategy previously demonstrated to be effective for reducing thermal gradients and defect density.[48]

Notably, this work leverages substrate preheating not only to mitigate defects but also to implement an in situ austempering treatment during printing. This approach enables, for the first time to our knowledge, the production of as-printed, nanostructured, carbide-free bainitic steels, eliminating the need for the post-processing heat treatments commonly required because of the high hardenability and cooling rates characteristic of these materials.

MATERIALS AND METHODS

Powder Characterization

In the current study, gas-atomized pre-alloyed powders of medium-carbon high-silicon steel, provided by Pometon S.p.A., were employed. The steel powder had an apparent density of 4.1 g/cm^3 measured following ASTM B212. Additionally, a Malvern laser-based particle size analyzer was utilized to measure the diameter size and distribution of the powder particles, which range between 15 and 53 lm. The chemical composition of the powders, determined via inductively coupled plasma mass spectrometry (ICP-MS), is reported in Table I. The powder morphology was examined using a Leo Stereoscan 440 scanning electron microscope (SEM). As shown in Fig. 1a, most powder particles displayed a regular spherical morphology, although a few irregular particles and satellites formed during the atomization process, highlighted by the red arrows. High-magnification SEM imaging (Fig. 1b) revealed micro-dendritic features on the particle's outer surface. To examine the cross-sections of the powder particles, the steel powders were mounted and polished according to the standard procedures and examined under SEM after chemical etching with Nital2 (2% nitric acid-98% ethanol) etching solution. The observation, displayed in Fig. 1c, revealed internal porosities, while the microstructure was identified as martensite (Fig. 1d), a result of the high cooling rate developed by the gas atomizing powders. Finally, Fig. 1 displays the backscattered SEM image accompanied by EDS elemental analysis. The EDS analysis indicated a homogeneous distribution of the alloying elements.

Design of the L-PBF Process

An Aconity Mini L-PBF system was employed to fabricate all specimens. The system is equipped with a continuous-wave IPG fiber laser, delivering a maximum power of 200 W, a built plate size of 140 mm diameter, and a buildable height of 190 mm. The adopted system was also characterized by a variable laser spot diameter, which in this study was fixed at 80 lm at the bed. The build platform was made of austenitic stainless steel 316L.

Table I. Chemical composition (wt.%) of the medium-carbon high-silicon steel powders adopted in this study measured with ICP-OES

Fe	C	Si	Mn	Al	O
Bal.	0.35	3.3	2.6	0.1	0.02

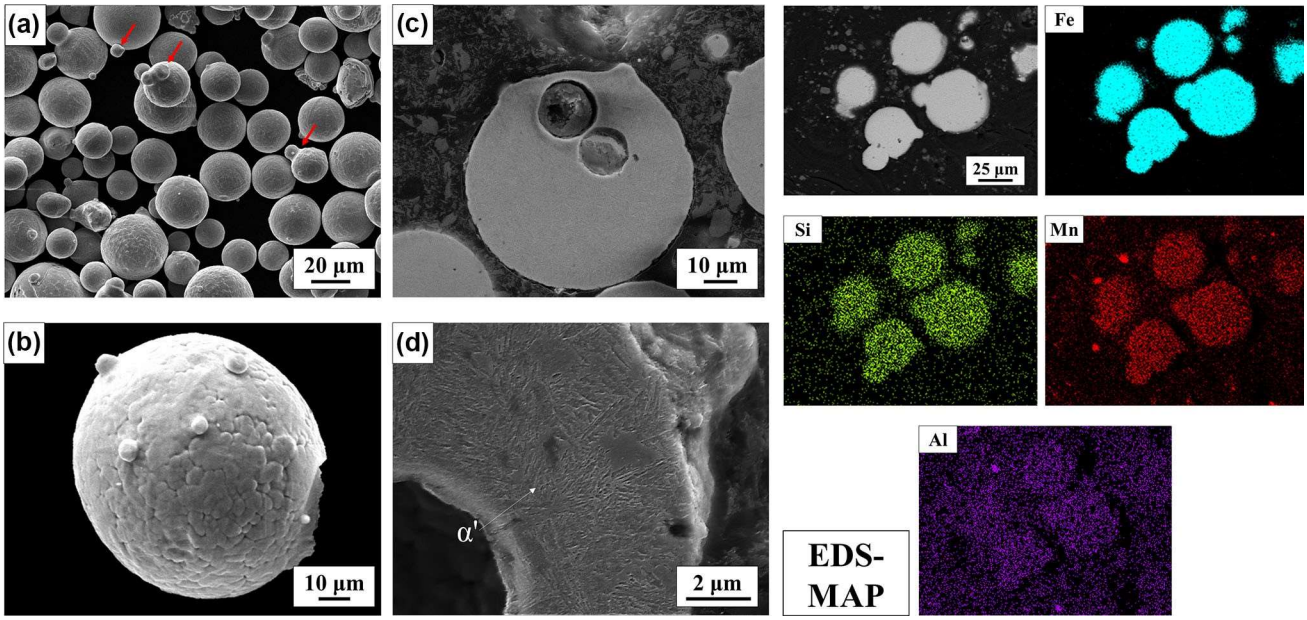

Fig. 1. (a) Secondary electron images showing the morphology of gas atomized powder medium carbon high silicon steel (red arrow indicates the satellites); (b) magnified surface image of the adopted powders showing the micro-dendritic features and small satellites; (c) SEM micrographs of the cross-section of the used powders showing internal porosities; (d) magnified SEM micrographs of the powder cross-section showing the martensitic (a') microstructure revealed by Nital etching and the EDS map carried out on the adopted gas atomized powders showing the elemental distribution of Fe, Si, Mn, and Al (Color figure online).

To identify suitable processing conditions for producing high-density parts, a preliminary parametric study was conducted by depositing single tracks. Laser power (P) was varied between 50 to 200 W, while the scan speed (v) ranged from 200 to 2000 mm/s, resulting in 53 parameter combinations that were adopted (appendix A, Table III). These combinations corresponded to line energy (EL), defined as EL = P/vs, ranging between 0.04 and 0.21 J/mm. The deposited single tracks (Fig. 2a) were analyzed via optical microscopy and based on thickness regularity and deposition continuity. A representative example of a regular and an irregular single track is shown in Fig. 2b–c. Twenty parameter sets were shortlisted for further fabrication for further parameter refinement, involving successive fabrication of 10 9 10 9 10 mm^3 cubes.

Final processing parameters included laser powers of 100, 150, 175, and 200 W and scan speeds of 400, 600, 800, 1000, 1200, 1400, and 1600 mm/s. The layer thickness (Z-increment) was equal to 30 lm and fixed for further fabrication, and the hatch distance was set to 80 µm.

All samples were built using a back-and-forth scan pattern for each layer. The entire pattern rotated by 90 (hatch angle) for each subsequent layer. This approach ensures uniformity after the deposition and melting of four-layer rows in each orientation. A schematic representation of the scan strategy is provided in Fig. 2d.

Initial sample fabrication was carried out without platform preheating, and no contour melting or support structures were applied to the building platform. The building chamber temperature was measured at around 25C. All builds were conducted under an argon atmosphere to maintain oxygen levels< 1 ppm. The fabrication parameters are summarized in Table II; the acronym NPH refers to the no-pre-heating condition.

In situ Heat Treatment Design

Considering the hardenability of the studied material,[42,43,49] the high cooling rates reached during the L-PBF process, and the previous results by the authors reported in Ref. 42, an as-print martensitic microstructure, comprising a mixture of fresh and tempered martensite, is expected. However, since the objective of this study is to obtain a bainitic microstructure, a second L-PBF fabrication campaign was carried out. As outlined in the previous sections, the bainitic microstructure is obtained using an austempering treatment, including austenitization and isothermal holding at a temperature close to Ms.[43,49,50] For this specific alloy, the suitable range for bainitic transformation is 300–350C.[50] Consequently, in the second set of experiments, the build platform was preheated and maintained at 320C throughout the entire fabrication process. After completion, the specimens were held at this temperature for an additional 1.5 h to ensure that each deposited layer,

and ultimately the entire component, remained within the bainitic transformation range. The final cooling was performed in air to room temperature. The processing parameters were identical to those used in the nonpreheated condition. In this case, however, the acronym PH (preheated) is used to identify the corresponding samples, replacing the previously used NPH (no preheating) designation.

Microstructural Characterization of L-PBF Built Samples

Cross-sections of the cube samples fabricated under different process conditions, with and without pre-heating and in situ and 200 9 from both the center and near-surface of the specimen, with a Leica DMRE optical microscope. These images were analyzed using ImageJ,[50] and statistical data treatment was conducted with OriginLab.[51] Notably, to eliminate excess impurities deriving from metallographic sample preparation, and considering solely the contribution of the porosity, the specimens underwent ultrasonic washing in a 10% ethanol solution in distilled and deionized water for 10 min and dried. Samples were then rinsed with acetone before optical microscopy observations.

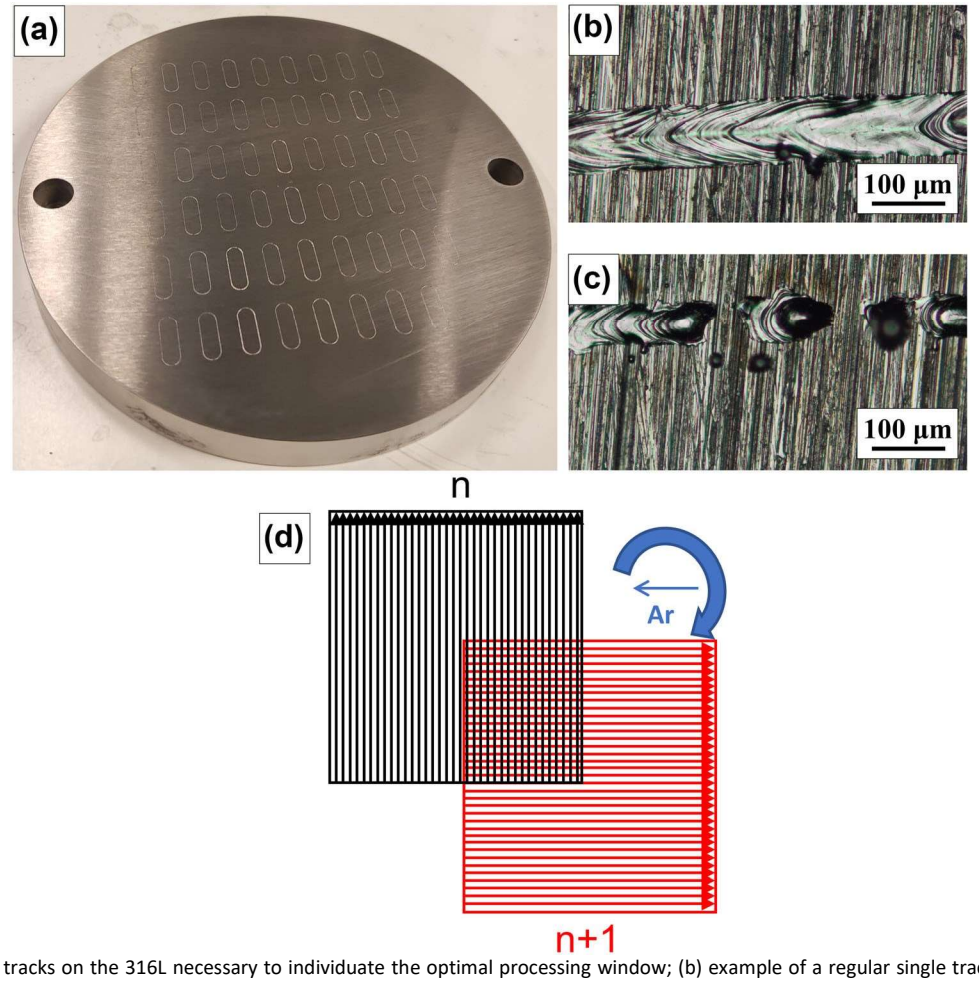

Fig. 2. (a) Deposited single tracks on the 316L necessary to individuate the optimal processing window; (b) example of a regular single track characterized by uniform thickness; (c) example of an irregular single track characterized by discontinuity and unmelted particles; (d) scheme of the adopted fabrication strategy.

Microstructural features of the as-built samples after polishing were revealed by chemical etching using Nital2 reagent (nitric acid: 2% in ethanol) and examined under both optical and SEM. TEM analysis was performed with a FEI Tecnai G2 TEM (FEI Co., Hillsboro, Oregon) microscope operating at 120 kV. TEM sample preparation included mechanical thinning to 50 lm with SiC abrasive papers, punching of 3-mm discs, and twin-jet electropolishing using a Struers Tenupol 3 system. A solution of 95% acetic acid and 5% perchloric acid served as the electrolyte at 45 V and room temperature.

Table II. Fabrication parameters selected for L-PBF fabrication, based on the analysis of the single-scan analysis

	Laser power (um)	Scan speed (mm/ (um)	Layer thickness mm^3)	Hatch distance	Energy density (J/ Sample (W)	s)
1-NPH	100	400	30	80	104.2	
2-NPH	100	600	30	80	69.4	
3-NPH	100	800	30	80	52.1	
4-NPH	150	400	30	80	156.3	
5-NPH	150	600	30	80	104.2	
6-NPH	150	800	30	80	78.1	
7-NPH	150	1000	30	80	62.5	
8-NPH	150	1200	30	80	52.1	
9-NPH	175	600	30	80	121.5	
10-NPH	175	800	30	80	91.4	
11-NPH	175	1000	30	80	72.9	
12-NPH	175	1200	30	80	60.8	
13-NPH	175	1400	30	80	52.1	
14-NPH	175	1600	30	80	45.6	
15-NPH	200	600	30	80	138. 9	
16-NPH	200	800	30	80	104.2	
17-NPH	200	1000	30	80	83.3	
18-NPH	200	1200	30	80	69.4	
19-NPH	200	1400	30	80	59.5	
20-NPH	200	1600	30	80	52.0	

Qualitative and quantitative phase analyses of the as-built fabricated specimen were performed by x-ray diffraction (XRD, Siemens D500) with Cu-Ka radiation (k = 1.54 A°), scanning over a 2h range of 40 to 105, with a step scan of 0.02. Quantitative analysis, including estimation of the retained carbon-enriched austenite volume fraction, was conducted using MAUD software.[52]

Nanoindentation measurements were carried out using an HYSITRON TI 950 TriboIndenterTM, equipped with a diamond Berkovich tip, to evaluate the hardness distribution across the deposited layers. Indentation mapping consisted of a series of indentations that were performed by imposing a penetration force of 150 mN. Indentations were spaced far enough apart so that the indentation behavior was not affected by the adjacent indentations according to the ISO standard 14577-4:2016. From the load and penetration depth, hardness was estimated using the standard Oliver and Pharr method.

RESULTS AND DISCUSSION

Fabrication with Parameter Optimization Without Pre-heating

Figure 3a presents the as-built fabricated specimens, with the dashed line indicating the crosssectioning plane.

Examination of the polished surfaces revealed different amounts of porosities (appearing as dark irregular areas) depending on the fabrication parameter. Notably, specimens fabricated using energy density values (VEDs)< 60 J/mm^3 and > 140 J/mm^3 exhibited abundant building defects, as illustrated in Fig. 3 b and c, and significant porosity levels [ranging from 1% to 3.8% (Fig. 4)]. Conversely, process parameter sets yielding VEDs between 60.8 and 138.8 J/mm^3 result in a reduced amount and size of the defects, which consist mainly of spherical gas porosities (Fig. 3b, d and e, blue arrows) and correspond to higher relative densities. At low VEDs, insufficient energy input results in limited melt pool formation, incomplete powder consolidation, and voids located near the melt pool boundaries. This condition is exacerbated by poor overlap between adjacent scan tracks, further reducing density. Moreover, in addition to gas porosity, lack-of-fusion (LoF) defects containing unmelted particles were observed within larger voids under low-energy conditions. On the other hand, energies > 140 J/mm^3 lead to a density reduction due to potential keyholing, material vaporization, and melt pool instability. Thes behaviors are supported by literature findings for ferrous[53] and non-ferrous alloys.[54] Finally, regardless of the input energy, the specimens exhibit cracks orthogonal to the building direction. These are attributed to the high cooling rates of the melt pools, in the order of 10^6-10^8 K/s,[48,55] and the thermal gradient > 10^4 K/mm.[56] High thermal stresses are generated, resulting in the formation of cracks (Fig. 3e, green arrows). In addition, as

reported by Ref. 57, a second contribution to the stresses developed during the fabrication is ascribed to the high material hardenability and the martensitic transformation that naturally occurs during cooling.[46] In fact, the volume expansion related to the martensite formation[58] introduces additional stresses into the material, which causes local failures. Crack initiation occurs near the rough side of the fabricated part, where the stress concentration is highest,[59] and propagates toward the center of the specimens. Moreover, in agreement with Chen et al.,[59] the cracks are mainly located in the lower part of the cubes, where the stress level reaches its maximum because of the largest temperature gradient. On the other hand, close to the top edges of the cubes, cracks were not detected, because at the free boundary, the stress is the lowest.[59]

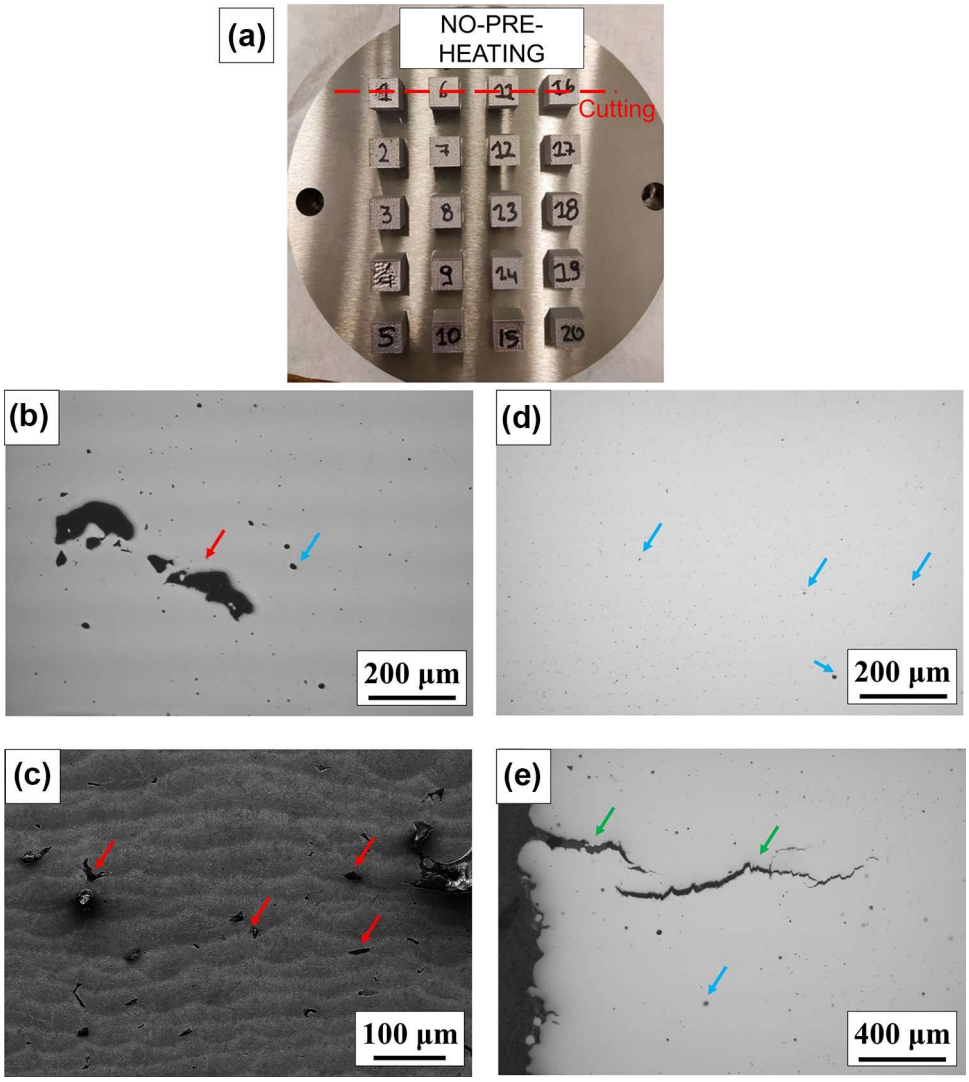

Fig. 3. (a) Overview of the fabricated NPH specimens (the red dashed line indicates the cutting section for the microstructural characterization); optical micrographs of the polished cross-sections of the as-built cubes displaying fabrication defects for the non-pre-heated specimens: (b) lack of fusion (red arrows); (c) defects located at the melt pool boundary (red arrows); (d) spherical gas porosities (blue arrows); (e) cracks in the cross-sectioned surface (green arrows) (Color figure online).

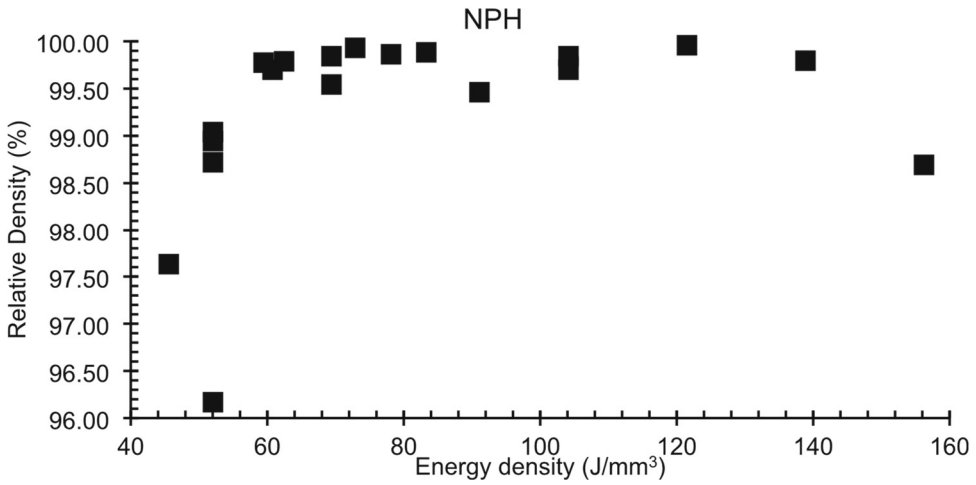

Fig. 4. Energy density (J/mm^3) vs experimentally determined relative density (%) plot for the specimen fabricated without platform pre-heating (NPH specimens).

Figure 5 presents the results of the statistical analysis of the pore surface area for the NPH specimens, derived from image analysis of multiple optical microscope images. Notably, the surface area was selected for this analysis rather than the diameter of the pores. This approach ensures the inclusion of irregularly shaped pores, which would not be adequately represented by a diameter-based metric. The findings indicate that the pore surface area reaches its minimum value for specimens numbered 9 to 14, underscoring this range as the optimal parameter window for the L-PBF (laser powder bed fusion) process. This range corresponds to the highest material density and the smallest pore sizes, signifying improved processing conditions and enhanced material quality.

Microstructural Characterization

Figure 6a displays an overview microstructure of the vertical (XZ plane) of the as-built specimens, with a magnified region provided in Fig. 6b. As shown in Fig. 6b, the layer thickness and the rotation angle between two subsequent layers are 30 lm and 90, respectively, consistent with the selected fabrication parameter and the adopted scan strategy. Notably, the top layer does not undergo further thermal cycling, as no additional material is deposited above it. Consequently, no tempering occurs in this region, resulting in a fresh, untempered martensitic microstructure, as shown in (Fig. 7c). In agreement with the previous attempt made by the same authors[46] and as expected from simulated CCT curves,[60] the solidification microstructure is fully austenitic, and upon cooling, the high achieved cooling rates and the high hardenability of the steel promote the martensitic formation. In Fig. 7a and b, the SEM micrographs show thin bright lines that represent the cellular structure and fine columnar prior austenite grains (indicated by the red arrows) growing from the melt pool boundary during the solidification process. The width of the columnar grains was 1 lm, with lengths extending through the layer. The etching also reveals a non-homogeneous microstructure across the various layers, as shown in the optical and SEM micrographs (Figs. 6b and 7c) by the appearance of alternating dark and bright etching areas. In the layer-by-layer L-PBF fabrication process, each deposited layer of material undergoes multiple complex thermal cycles, similar to a welding process, creating heat-affected zones (HAZ) in the vicinity of the melt pool boundary and the layer core. Upon deposition of the (n + 1) layer, the newly formed layer solidifies rapidly, leading to marten site formation. Meanwhile, the material deposited in the underlying n layer surrounding the melt pool boundary is exposed to high temperature, higher than the critical Ac3, leading to the austenitization that will transform again into fresh martensite upon cooling. Conversely, the inner part of the layer is reheated at a temperature below Ac3 in the biphasic region, or below Ac1, leading to the formation of a dual-phase microstructure in the first case and simple tempering of the microstructure in the second case, which is less hard. TEM observation on sample 17-NPH provides high-resolution insights into the as-built microstructure (Fig. 8). In Fig. 8a and b, the micrographs show laths of martensite with retained austenite sandwiched between the laths corresponding to the melt pool core

As discussed by the author in a previous analysis,[46] this microstructure is not the desired one, and it is not suitable for the possible final application. This introduces the need for further post-processing and austempering treatments to achieve the desired mechanical properties. Phase analysis of the asbuilt sample was carried out using x-ray diffraction, and reflections of both martensite and austenite are observable, with a volume fraction of austenite varying between 10 and 30%, however, without any evident correlation between the process parameters. The significant amount of retained austenite is the consequence of the multiple phenomena occurring during the fabrication. On one hand, thermal cycles experienced by the

deposited material, the formation of a possible dual-phase microstructure, and the carbon partitioning stimulated by the reheating contribute to increasing the austenite stability. On the other hand, mechanical stabilization phenomena are associated with high cooling rates, large dislocation densities typical of the fabrication process, and phase transformations. The martensitic transformation is displacive in nature, and the consequent austenite work hardening induced by the developed strain and the introduction of dislocations can enhance the challenge of sub-unit propagation, despite some new dislocations potentially serving as sites for nucleation. The motion of glissile interfaces can be impeded and transition to a sessile state because the newly introduced dislocations hinder the formation of bainite or martensite.[40,43] In addition, the variation in the volume fraction may also be related to the platform location of the various cubes, whose effects have been explored in the existing literature.[61–65] However, this is not the object of the present research.

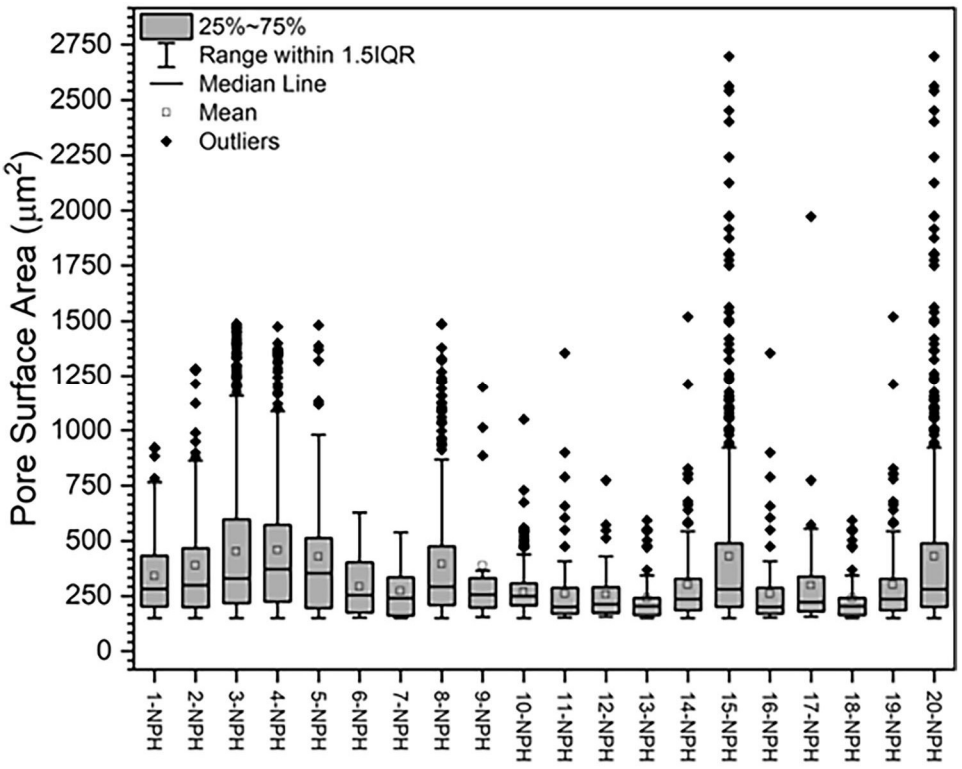

Fig. 5. Results of the statistical analysis carried out on the fabrication defects (pore surface area) detected on the NPH specimens derived from image analysis of optical microscope images acquired on the specimen cross-section, parallel to the building direction

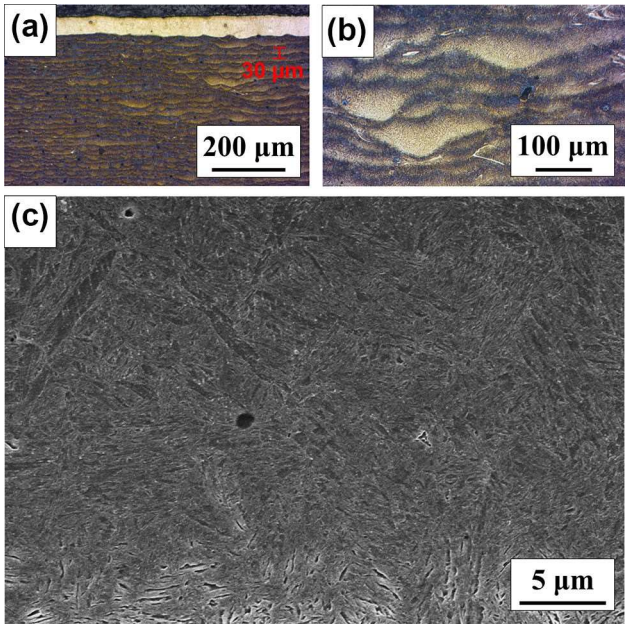

Fig. 6. (a) Optical micrograph showing an overview of the specimen microstructure along the building direction and revealing the layers in the as-fabricated specimen; (b) magnified view of the fabricated layers; (c) high magnification SEM micrograph displaying the martensitic microstructure of the last fabricated layer (top layer).

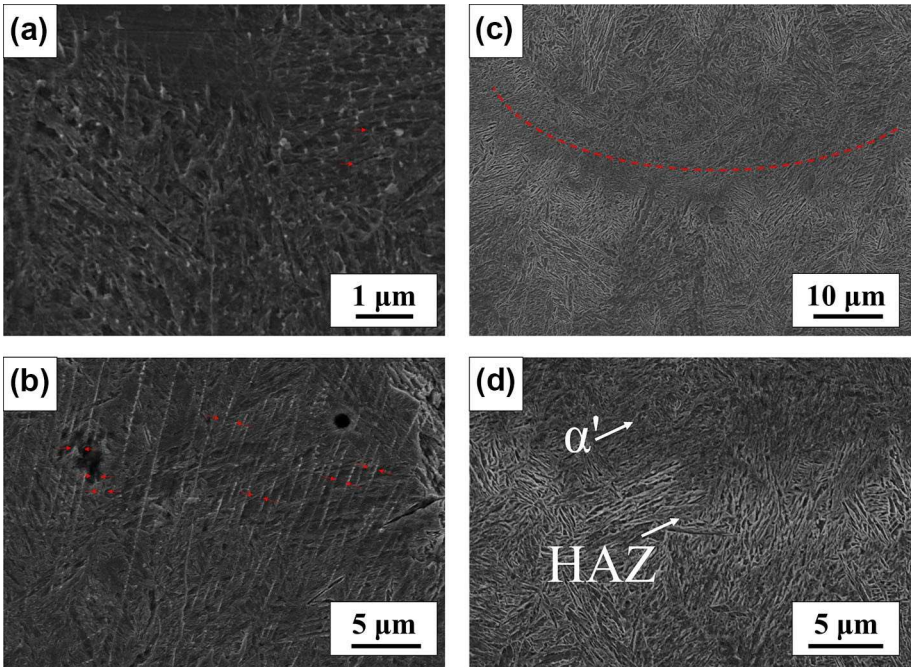

Fig. 7. (a) and (b) SEM micrographs showing the cellular structure formed during the solidification; (c), (d) SEM micrographs illustrating the microstructure in the inner and at the boundary of the melt pool, showing the presence of a heat-affected zone (HAZ) formed because of the deposition of subsequent layers.

.

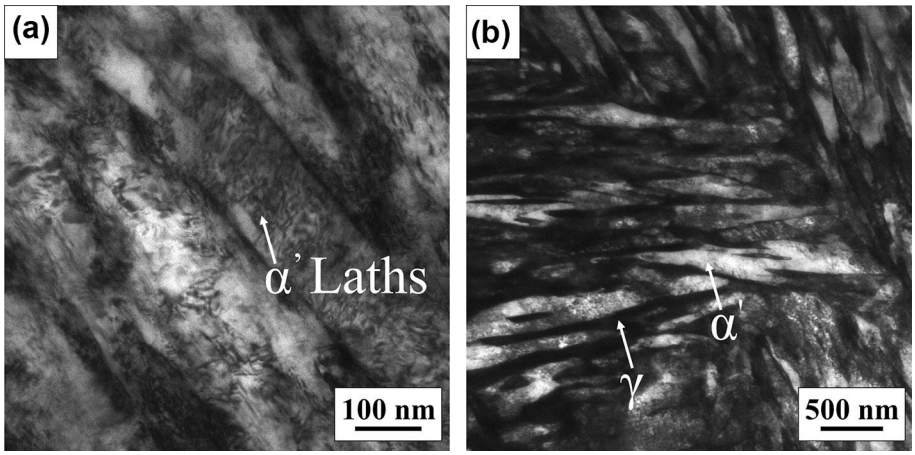

Fig. 8. TEM micrographs acquired on specimen 17-NPH (a) showing the martensite laths (a′) at the inner part of the melt pool; (b) detail showing the presence of retained austenite (c) located between the martensitic laths.

In addition, the EDS mapping of the as-built samples shows a uniform distribution of the elements, without evident macroscopic segregations. Due to the nature of point-by-point and layer-bylayer deposition of the process and the uniformity of the formed powder composition, as shown before, it was ensured that macroscopic segregation would not occur during the solidification process or that it would be confined in the short range. An example is depicted in Fig. 9. While no large scale segregation was observed, the possibility of microscale elemental segregation influencing local phase transformations cannot be excluded and would require advanced characterization techniques for definitive assessment.

Fabrication Including Pre-heating and In situ Heat Treatment: Effect on the Densification Behavior

The densification behavior of the samples was first investigated to assess the effect of substrate preheating on the L-PBF process. During the rapid and repeated local heating and cooling cycles intrinsic to L-PBF, during which the material is subjected during the process, several problems may arise, such as thermal gradients, resulting in thermal stresses. As shown in Fig. 3, these stresses lead to the formation of cracks within the fabricated components. Among the advantages of the platform pre-heating is the ability to produce ‘‘quasi crackfree microstructures,’’ since the thermal gradient experienced by the fabricated part is lowered and martensite formation is prevented.[66] Furthermore, as reported by Kempen et al.,[67] platform preheating has a positive effect on the resulting part density. Substrate pre-heating, during the L-PBF process, also mitigates the Marangoni effect, since it reduces the laser energy required to melt the powder bed. As reported by Zhou et al.,[68] the reduction in Marangoni effects results in the mitigation of the interaction between the recoil pressure and surface tension, so that the liquid cannot be pushed up and out of the depression. Therefore, a keyhole cannot be generated at the bottom of the melt pool, so the number of keyhole defects in the specimens prepared with substrate preheating is also reduced.

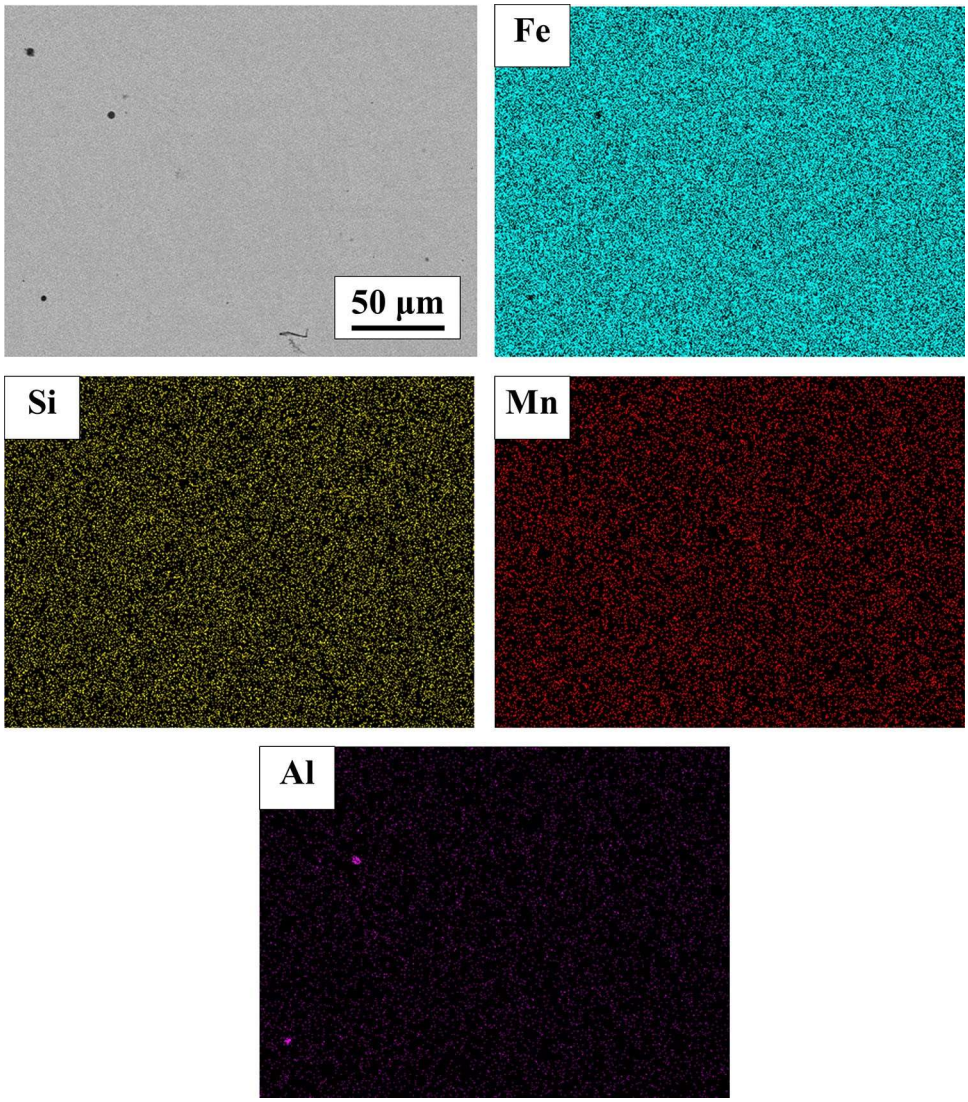

Fig. 9. Example of an EDS map on the as-built NPH sample, along the building direction, showing uniform element distribution of Fe, Si, Al, and Mn in the samples.

As reported by Park et al.,[69] substrate pre-heating aids in removing moisture from the powder, enhances powder spreadability,[70] prevents powder oxidation, and improves the energy density efficiency. These effects contribute to lower incidence and smaller size of the defects, as illustrated in Fig. 10, corroborating the previous results found by the same authors in a previous attempt. Further details are included in Appendix A (Table IV), where the statistical analysis is reported.[69]

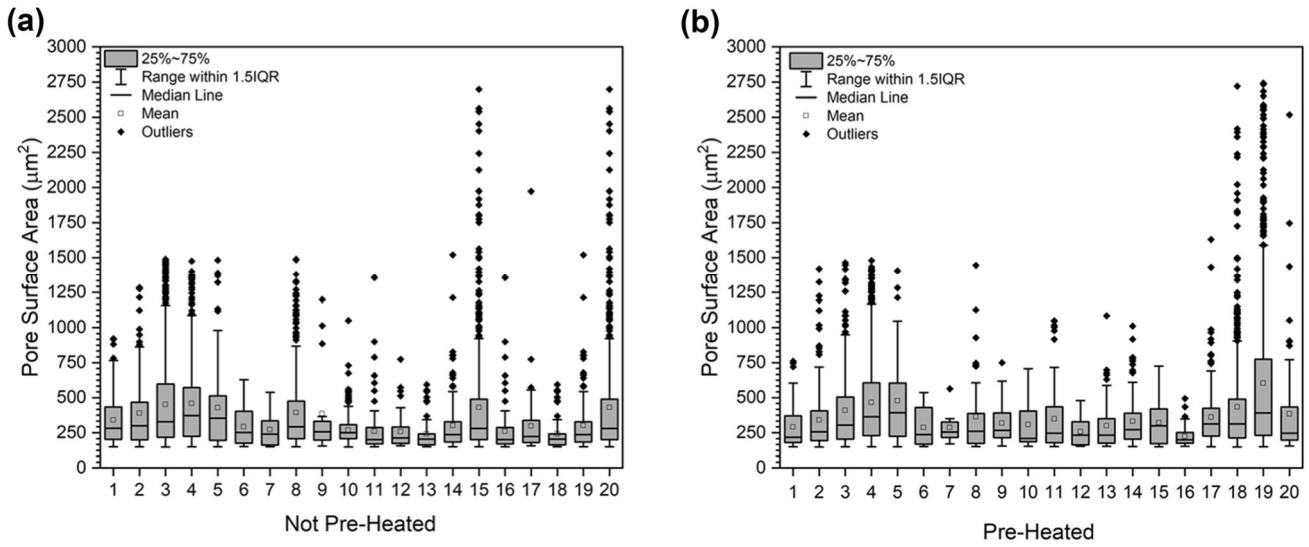

Fig. 10. Comparison of the results of the statistical analysis (carried out on the micrographs acquired using optical microscopy) on the pore surface area for the NPH specimens and those fabricated with the platform pre-heated to PH.

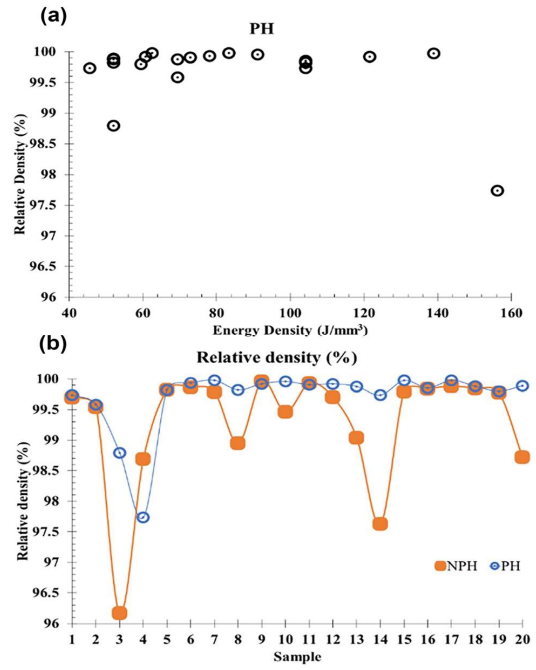

Fig. 11. (a) Plot showing the effect of input energy density on the relative density (%) of the PH specimens; (b) comparative plot of the relative density of the fabricated specimen without platform preheating (NPH) and with pre-heating (PH).

The statistical analysis of the pore surface area conducted on all specimens fabricated by platform pre-heating confirms that the parameters selected for the L-PBF process can be optimized to significantly reduce both the total number of defects and the pore surface area. This optimization yields specimens with increased density and improved overall quality. As illustrated in Fig. 10 and, in more detail in Appendix A (Table IV), specimens within the range of 7 to 16 exhibited the lowest total number of defects and statistically smaller pore surface areas compared to other samples, highlighting the effectiveness of the selected parameter range. These findings underscore the crucial roleMoreover, aligned with the results obtained by Kempen et al.,[67] the pre-heating positively influences the part density across all the energy density levels, leading to an overall improvement, as shown in Fig. 11. However, small of platform preheating on the quality of the processed parts, particularly in minimizing porosity. The reduction in porosity is directly associated with improved mechanical and functional performance, reinforcing the necessity of carefully controlled preheating in achieving high-quality L-PBF components.

Moreover, aligned with the results obtained by Kempen et al.,[67] the pre-heating positively influences the part density across all the energy density levels, leading to an overall improvement, as shown in Fig. 11.hot cracks were detected in the cross-section of the specimens (Fig. 12). Explicative color maps are reported in Appendix A (Fig. 16).

Fabrication Including Pre-heating and In situ Heat Treatment: Effect on the Microstructure

Similarly to the NPH specimens, the distribution of the alloying elements in the preheated specimens was investigated using SEM-EDS, revealing a uniform distribution of the major elements.

Figure 13a shows the typical microstructure of the conventional material, identical in chemical composition, fabricated by casting and hot rolling, after isothermal treatment at 320C for 3 h. The microstructure consists of nanoscaled bainitic ferrite (< 100 nm) and carbon-enriched austenite with film and block morphology. Figure 13b shows the microstructure of the vertical (XZ-plane) of a specimen fabricated with substrate preheating and in situ austempering treatment. Similarly, these specimens exhibit a carbide-free bainitic microstructure, consisting of bainitic ferrite and retained austenite, with both film and block morphology, in agreement with that observed in the conventional material treated with austempering at the same isothermal transformation condition. The absence of a predominant martensitic microstructure, which is typical of the sample obtained without preheating (Fig. 7), confirms the effective capacity to avoid the layer-by-layer quenching of the material, thereby promoting bainite formation.

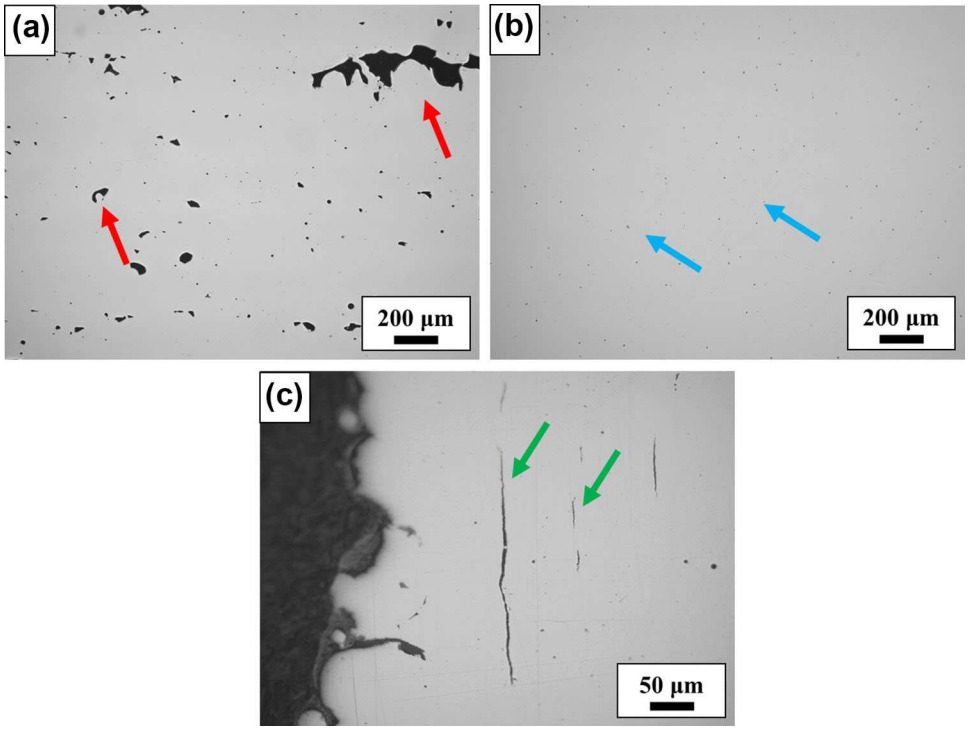

Fig. 12. Optical micrographs acquired on the polished cross-sections of the as-built cubes displaying fabrication defects on the pre-heated specimens (PH): (a) lack of fusion (red arrows); (b) spherical gas porosities (blue arrows); (c) cracks in the cross-sectioned surface (green arrows) (Color figure online).

A closer examination of the microstructure (Fig. 13c and d) shows the presence of grain boundaries, highlighted by the red arrows and circles, which, similar to the fabrication without pre-heating, are related to the cellular structure generated during the solidification process. This leads, as shown in Fig. 13, to the variation in the morphology of bainitic ferrite and the retained austenite compared to the bulk material prepared through conventional methods. Some of the specimens, in addition to bainitic ferrite and carbonenriched austenite, also showed the presence of small martensitic islands, formed during final cooling to room temperature. So far, this might be attributed to local segregation and chemical composition inhomogeneities, undetectable via conventional EDS mapping—as well as differences in platform location, which can affect energy input and thermal profiles, as reported by Ref. 61.

TEM micrographs of Fig. 13e–h on the specimen 17PH show a detail of the films of retained austenite embedded between the bainitic ferrite sub-units. Furthermore, carbides were not detected, despite the long duration of the fabrication process at 320C, because of the bainitic microstructure's high resistance to tempering Ref. 49.

XRD measurements, conducted parallel to the build direction, confirmed the presence of retained austenite and tetragonal body-centered phases across all specimens. Notably, in most of the samples, the peak intensity of c (200) in L-PBFfabricated samplesis higher than that of the conventionally fabricated and austempered material and other fabricated specimens, suggesting the presence of textures. Furthermore, the Rietveld refinement shows that irrespective of the process parameters, the amount of carbon-enriched retained austenite (Vc) lies again between 10 and 30%, with a carbon content estimated from the lattice parameters, according to Cheng et al.,[71] of 1.1–1.25 wt.%, similar to the conventional bulk steel with the same chemical composition and the same isothermal transformation conditions.[49] Similarly, the carbon content of bainitic ferrite was found to be > 0.13%, which is not surprising considering the tetragonal distortion. Additionally, the presence of martensite in some of the specimens contributes to the increase in overall carbon content. The values of the austenite volume fraction in each specimen are reported in Appendix A (Table V).

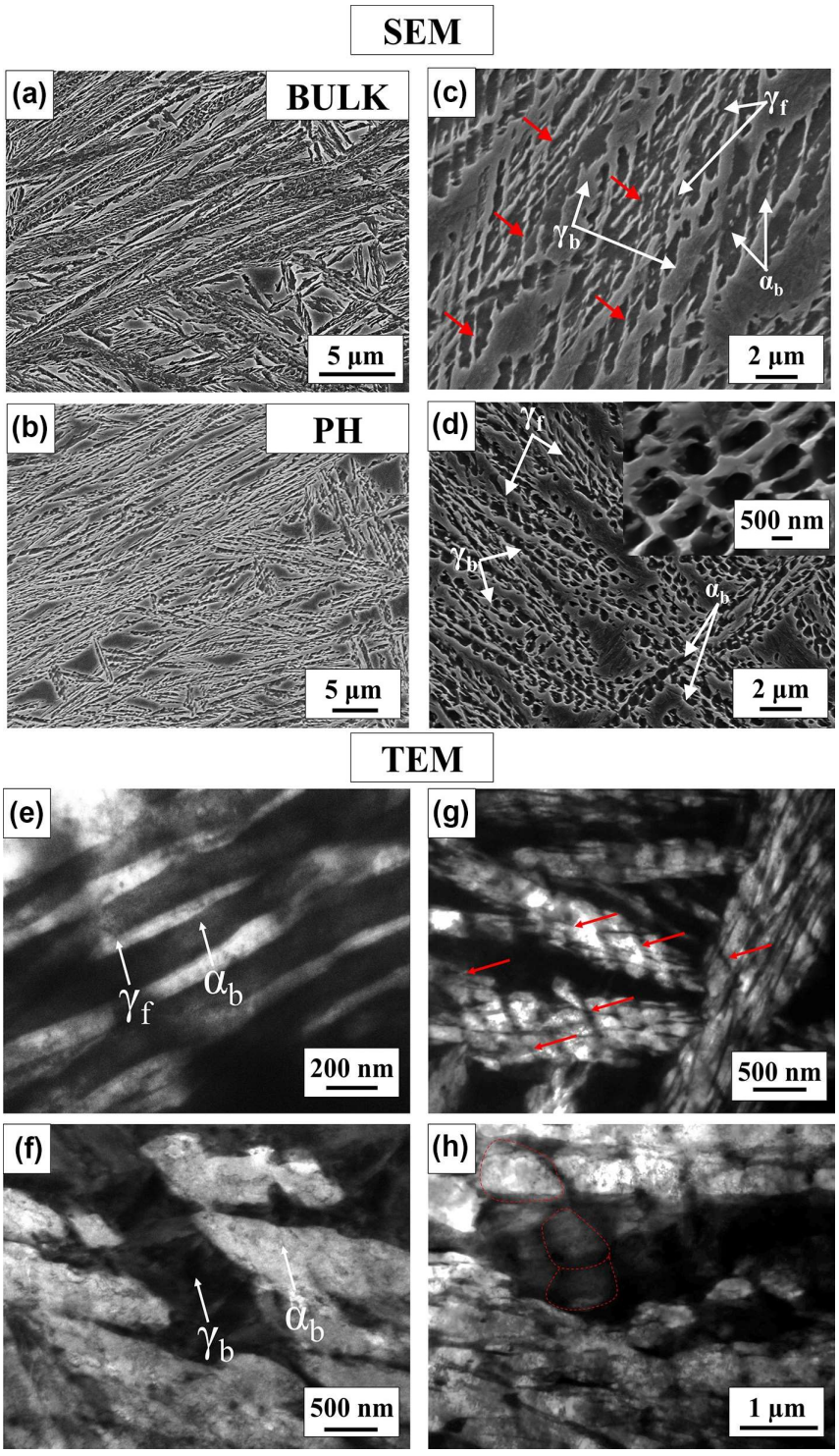

Fig. 13. SEM micrographs illustrating (a) the conventionally fabricated material (cast, hot rolled, and austempered) with analogous chemical composition after isothermal holding to develop the bainitic microstructure, consisting of nanoscale bainitic ferrite, (b) LPBF fabricated with preheating (16 PH specimen) in as-fabricated condition, (c) and (d) magnified SEM micrographs of the as-fabricated specimen with pre-heating, (e–h) TEM micrographs of the as-fabricated specimen with pre-heating (16 PH).

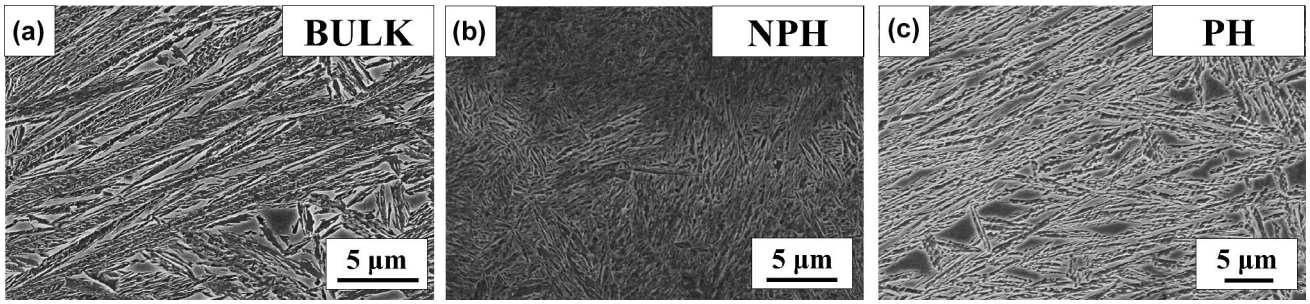

Fig. 14. Summary of the microstructure for the (a) bulk material after austempering to develop bainitic microstructure, (b) L-PBF NPH specimen in the as-fabricated condition with a microstructure consisting of fresh and tempered martensite with retained austenite, and (c) L-PBF PH in the as-fabricated condition showing a bainitic microstructure.

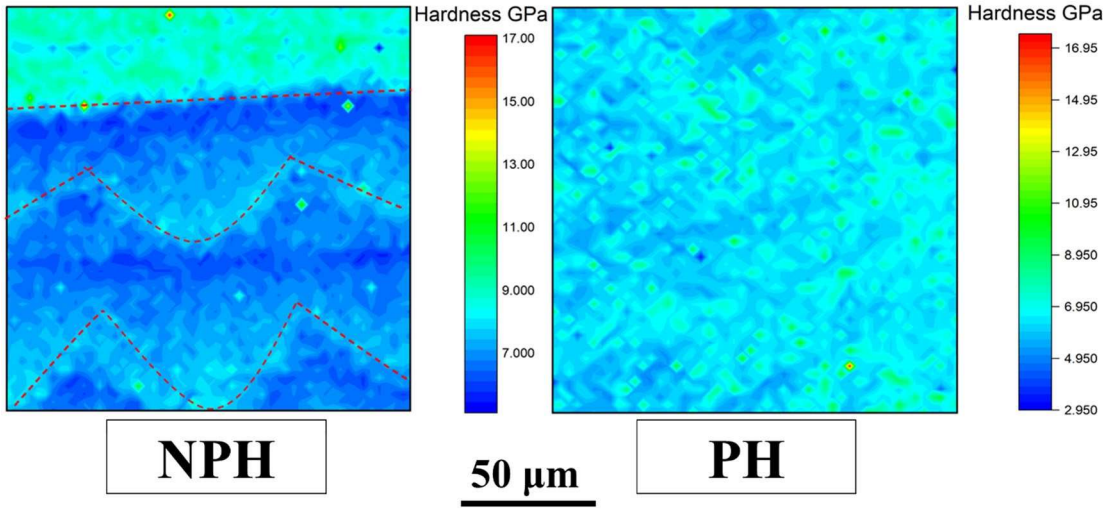

Fig. 15. Nanohardness maps recorded on the 16 NPH and 16PH specimen in the as-fabricated condition along the as-build direction.

Finally, although SEM, TEM, and XRD did not detect the presence of carbides, it is worth noting that, despite the high silicon content, the existence of nanoscale transition carbides or cementite cannot be excluded. As shown by Rementeira et al., such phases may exist below the detection threshold of conventional techniques.[72]

A final summary of the microstructure is reported in Fig. 14, showing that the samples produced with pre-heating (Fig. 14 c) are characterized by a similar bainitic microstructure to the conventional material after heat treatment (Fig. 14a) and different microstructures compared to the one printed without pre-heating (Fig. 14b), which instead presents a martensitic structure. This shows that the use of pre-heating is an interesting approach to perform in situ heat treatment and thus obtain the desired bainitic microstructure directly after printing.

Nanohardness Measurements

The hardness of the fabricated samples was evaluated using nanoindentation testing to compare the two fabrication approaches adopted in this study (with and without pre-heating), thereby supporting the interpretation of the microstructural observations. The main results are summarized in Fig. 15. For the NPH specimens, the resulting hardness map reveals clear inhomogeneities corresponding to the microstructural variations previously observed via SEM analysis. In particular, the last deposited layer is distinctly identifiable and exhibits the highest hardness, attributed to its fresh, untempered martensitic microstructure. Similarly, moving downward, toward the specimen base, the hardness distribution reflects the variation in the microstructural constituents found across the single layer. Specifically, higher hardness values are observed near the melt pool boundaries, where the material is more likely to undergo re-austenitization during

subsequent layer deposition and transform again into martensite upon cooling. Conversely, the inner regions of each layer, which do not reach temperatures above the Ac3 threshold, experience only tempering, resulting in comparatively lower hardness. In contrast, while pre-heating coupled with the in situ heat treatment is applied during the fabrication, the hardness appears more homogeneous and generally lower because of the developed microstructure. The preheating and isothermal holding at 320C cause the austenite formed during solidification in each deposited layer and in the heat-affected zone after a new deposition to transform into a mixture of bainitic ferrite and carbon-enriched austenite. Moreover, the values aligns with similar measurements in the same chemical composition produced by conventional fabrication methods, e.g., casting and hot working, subjected to austempering treatment at similar temperatures.[50] For the same reason, a top layer with a different microstructure and hardness has not been detected.

Summarizing the results of the present paper. the presence of the pre-heating of the platform at 320 facilitated the LPBF fabrication of bainitic steel for several reasons linked to both the manufacturing process and the metallurgical characterization. Considering the manufacturing process, pre-heating allows widening of the range of parameters suitable to minimize the pore surface area (samples 9-14 in the cases without pre-heating, samples 7-16 in samples with pre-heating) and generally positively influences the density of the samples across all the energy density levels. Considering the microstructural features, the presence of pre-heating permits directly obtaining the desired bainitic microstructure in the as-printed condition thanks to the in situ heat treatment that occurs, whereas without preheating the microstructure resulting primarily from martensite requires a further heat treatment, lasting some hours, to transform into bainite. Considering both factors, the use of proper pre-heating of the platform can enhance the possible technological application of the LPBF process to bainitic steels.

CONCLUSION

In this work, the fabrication of a nanostructured bainitic steel was performed with and without substrate pre-heating. The fabrication parameter was optimized in both conditions to achieve high relative densities (> 99%). The application of the substrate pre-heating was introduced to mitigate the thermal gradients and reduce the defects naturally induced by the additive manufacturing process and to exploit the austenitic solidification structure and maintain it at a temperature suitable to develop a nanostructured bainitic microstructure.

The key findings of this study can be summarized as follows:

- Substrate pre-heating followed by isothermal holding at 320C significantly enhances densification while reducing the number and size of defects, such as lack of fusion and gas porosities.
- The mitigation of thermally induced stresses, enabled by the pre-heated substrate, prevents the formation of cracks and preserves the structural integrity of the fabricated specimens.
- For the first time to our knowldege, it was demonstrated that a nanostructured bainitic microstructure, comprising bainitic ferrite and carbon-enriched retained austenite, can be achieved directly during the fabrication process, eliminating the need for post-fabrication heat treatments.
- Microscale investigations of the bainitic microstructure revealed morphological differences between conventionally fabricated microstructures and those produced via additive manufacturing. These differences are attributed to the cellular hierarchical structures, characteristic of the additive manufacturing process.

ACKNOWLEDGEMENTS

M. Franceschi thanks the European UnionNextGenerationEU, in the frame of the project iNEST-Interconnected Nord-Est Innovation Ecosystem (iNEST ECS00000043–Spoke 5*). E. Saggionetto and A. Mertens acknowledge the support of the FNRS (Fonds National de la Recherche Scientifique of Belgium, under PDR no. 35298295).

CONFLICT OF INTEREST

On behalf of all authors, the corresponding author states that there is no conflict of interest.

APPENDIX

See Tables III, IV, V and Fig. 16.

Table III. Single Track Parameters

Single track	Laser power (W)	Speed (mm/s)	Energy (J/mm)	Track width (um)
1	50	200	0.25	98.5
2	50	400	0.125	76.5
3	50	600	0.083333333	65.33333333
4	50	800	0.0625	54.5
5	50	1000	0.05	66
6	50	1200	0.041666667	55
7	100	200	0.5	153.5
8	100	400	0.25	124.6
9	100	600	0.166666667	99
10	100	800	0.125	91.57142857
11	100	1000	0.1	84.14285714
12	100	1200	0.083333333	73.46153846
13	100	1400	0.071428571	70.6
14	100	1600	0.0625	65.75
15	100	1800	0.055555556	65.72727273
16	100	2000	0.05	70.25
17	150	200	0.75	221.9
18	150	400	0.375	155.8888889
19	150	600	0.25	128.6
20	150	800	0.1875	116.1818182
21	150	1000	0.15	97.33333333
22	150	1200	0.125	97
23	150	1400	0.107142857	98.5
24	150	1600	0.09375	92.33333333
25	150	1800	0.083333333	80
26	150	2000	0.075	74.33333333
27	175	200	0.875	244.6666667
28	175	400	0.4375	197
29	175	600	0.291666667	144
30	175	800	0.21875	122.3333333
31	175	1000	0.175	108.5
32	175	1200	0.145833333	101
33	175	1400	0.125	95.33333333
34	175	1600	0.109375	90.33333333
35	175	1800	0.097222222	85.33333333
36	175	2000	0.0875	81.33333333
37	185	600	0.308333333	137
38	185	800	0.23125	131.25
39	185	1000	0.185	115
40	185	1200	0.154166667	108

41	185	1400	0.132142857	98.66666667
42	185	1600	0.115625	95.33333333
43	185	1800	0.102777778	87
44	200	200	1	258.75
45	200	400	0.5	188.6666667
46	200	600	0.333333333	161
47	200	800	0.25	129
48	200	1000	0.2	117.5
49	200	1200	0.166666667	117.6666667
50	200	1400	0.142857143	118
51	200	1600	0.125	89.33333333
52	200	1800	0.111111111	93
53	200	2000	0.1	88

Table IV. Summary of the statistical analysis of the fabricated specimen without pre-heating (NPH) and with pre-heating (PH)

Sample	N total	Mean	Standard deviation	Median	Interquartile (Q3–Q1)
1-PH	82.0	289.9	154.2	217.4	189.6
2-PH	172.0	340.5	233.4	256.7	212.5
3-PH	328.0	409.7	279.2	304.6	300.3
4-PH	923.0	465.2	302.0	363.4	377.5
5-PH	46.0	477.6	324.4	392.3	379.3
6-PH	19.0	288.1	133.8	236.3	261.4
7-PH	11.0	288.0	106.6	254.9	109.4
8-PH	43.0	363.5	278.1	260.1	213.6
9-PH	35.0	318.3	149.7	267.6	176.9
10-PH	21.0	307.3	182.5	210.0	220.3
11-PH	81.0	348.4	237.3	246.1	256.8
12-PH	14.0	257.4	108.6	232.3	165.2
13-PH	59.0	299.2	178.7	233.2	173.7
14-PH	117.0	331.6	184.0	271.7	184.9
15-PH	59.0	321.5	155.3	299.7	247.9
16-PH	52.0	222.9	71.3	198.8	75.7
17-PH	199.0	360.4	206.7	313.2	198.1
18-PH	522.0	432.6	372.0	312.0	277.3
19-PH	895.0	603.7	537.8	391.0	542.2
20-PH	95.0	384.5	349.5	246.4	235.4
1-NPH	132.0	339.6	182.1	281.7	230.0
2-NPH	146.0	389.3	256.4	298.7	268.6
3-NPH	1145.0	451.7	312.2	328.9	379.6
4-NPH	508.0	458.0	293.9	371.9	347.3
5-NPH	76.0	428.2	319.6	354.0	317.6
6-NPH	43.0	292.0	129.1	252.5	227.4
7-NPH	19.0	272.3	127.6	239.1	173.3
8-NPH	390.0	395.0	272.6	292.7	267.6
9-NPH	16.0	386.6	330.0	256.9	134.5
10-NPH	399.0	268.0	94.7	250.3	100.5
11-NPH	97.0	259.8	171.0	201.0	117.2

12-NPH	60.0	256.7	120.7	212.4	116.2
13-NPH	62.0	241.4	114.8	203.6	78.1
14-NPH	148.0	300.9	195.0	236.6	144.1
15-NPH	676.0	430.2	385.8	281.1	289.1
16-NPH	97.0	259.8	171.0	201.0	117.2
17-NPH	76.0	297.3	232.2	222.4	156.6
18-NPH	62.0	241.4	114.8	203.6	78.1
19-NPH	148.0	300.9	195.0	236.6	144.1
20-NPH	676.0	430.2	385.8	281.1	289.1

Table V. XRD results of the Rietveld analysis carried out on the XRD patterns acquired on the PH specimens

Sample	Vc (vol.%)
1PH	20.5
2PH	13.9
3PH	20.4
4PH	12.9
5PH	9.5
6PH	30.9
7PH	21.4
8PH	23.4
9PH	13.8
10PH	27.7
11PH	25.5
12PH	21.3
13PH	16.2
14PH	24.8
15PH	23
16PH	22
17PH	23
18PH	25.1
19PH	39.8
20PH	23.7

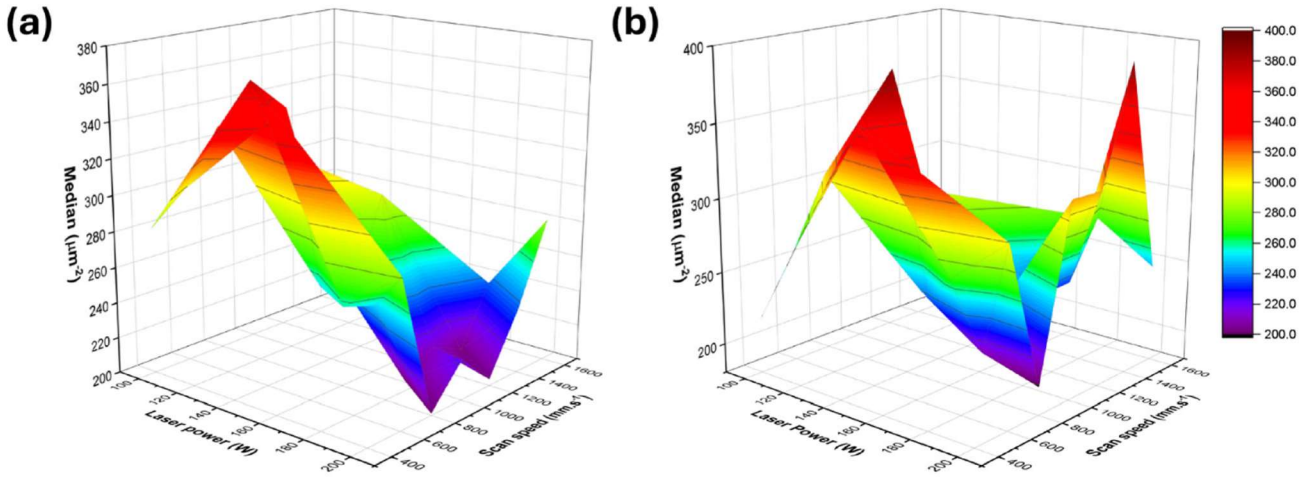

Fig. 16. Three-dimensional plot showing the effect of laser power and scan speed on the median pore surface area.

REFERENCES

1. S.L. Sing, and W.Y. Yeong, Virtual Phys. Prototyping 15, 359–370 https://doi.org/10.1080/17452759.2020.1779999 (2020).
2. A. Gisario, M. Kazarian, F. Martina, and M. Mehrpouya, J. Manuf. Syst. 53, 124–149 https://doi.org/10.1016/j.jmsy.201 9.08.005 (2019).
3. K. Kosiba, T. Gustmann, J.T. Kim, J. Seok, J. Jung, L. Beyer, S. Scudino, L. Giebeler, J. Han, and J.K. Hufenbach, J. Alloys Compd. 967, 171773 https://doi.org/10.1016/j.jallcom. 2023.171773 (2023).
4. S. Cooke, K. Ahmadi, S. Willerth, and R. Herring, J. Manuf. Process. 57, 978–1003 https://doi.org/10.1016/j.jmapro.2020. 07.025 (2020).
5. C.Y. Yap, C.K. Chua, Z.L. Dong, Z.H. Liu, D.Q. Zhang, L.E. Loh, and S.L. Sing, Appl. Phys. Rev. https://doi.org/10.1063/ 1.4935926 (2015).
6. W.E. King, A.T. Anderson, R.M. Ferencz, N.E. Hodge, C. Kamath, S.A. Khairallah, and A.M. Rubenchik, Appl. Phys. Rev. https://doi.org/10.1063/1.4937809 (2015).
7. J. Zhang, B. Song, Q. Wei, D. Bourell, and Y. Shi, J. Mater. Sci. Technol. 35, 270–284 https://doi.org/10.1016/j.jmst.201 8.09.004 (2019).
8. L. Pezzato, C. Gennari, M. Franceschi, K. Brunelli, Sci. Rep. (2022).
9. T. Wegener, J. Koopmann, J. Richter, P. Krooß, and T. Niendorf, Fatigue Fract. Eng. Mater. Struct. 44, 2570–2590 https://doi.org/10.1111/ffe.13527 (2021).
10. C. Wallis, and B. Buchmayr, Mater. Sci. Eng. A 744, 215–223 https://doi.org/10.1016/j.msea.2018.12.017 (2019).
11. H. Eskandari Sabzi, Mater. Sci. Technol. 35, 875–890 http s://doi.org/10.1080/02670836.2019.1602974 (2019).
12. A. Yazdanpanah, M. Franceschi, R.I. Revilla, S. Khademzadeh, I. De Graeve, and M. Dabala`, Corros. Sci. http s://doi.org/10.1016/j.corsci.2022.110642 (2022).
13. A. Yazdanpanah, R.I. Revilla, M. Franceschi, A. Fabrizi, S. Khademzadeh, M. Khodabakhshi, I. Graeve-, and Dabal M, Electrochim. Acta. https://doi.org/10.1016/j.electacta.2023.1 43723 (2024).
14. S. Khademzadeh, Prog. Addit. Manuf. (2021).
15. A. Girotto, M. Ballan, P. Rebesan, R. Dima, A. Monetti, I. Bodini, D. Paderno, V. Villa, A. Pepato, and M. Manzolaro, J. Phys. Conf. Ser. https://doi.org/10.1088/1742-6596/2687/8/ 082047 (2024).
16. P. Rebesan, M. Ballan, M. Bonesso, A. Campagnolo, S. Corradetti, R. Dima, C. Gennari, G.A. Longo, S. Mancin, M. Manzolaro, et al., Addit. Manuf. 47, 102277 https://doi.org/ 10.1016/j.addma.2021.102277 (2021).
17. C. Zitelli, P. Folgarait, and A. Di Schino, Metals. https://doi. org/10.3390/met9070731 (2019).
18. L. Wu, S. Das, W. Gridin, S. Leuders, M. Kahlert, M. Vollmer, and T. Niendorf, Adv. Eng. Mater. https://doi.org/10. 1002/adem.202100049 (2021).
19. L. Zai, C. Zhang, Y. Wang, W. Guo, D. Wellmann, X. Tong, and Y. Tian, Metals 10, 1–25 https://doi.org/10.3390/met10 020255 (2020).
20. B. Mooney, and K.I. Kourousis, Metals 10, 1–22 https://doi. org/10.3390/met10091273 (2020).
21. A. Santana, A. Eres-Castellanos, J.A. Jimenez, R. Rementeria, C.G. Capdevila, and F. Caballero, J. Mater. Res. Technol. 25, 6898–6912 https://doi.org/10.1016/j.jmrt.2 023.07.114 (2023).
22. A. Yazdanpanah, M. Franceschi, G. Bergamo, M. Bonesso, and M. Dabala`, Eng. Fail. Anal. https://doi.org/10.1016/j.e ngfailanal.2022.106192 (2022).
23. F. Deirmina, N. Peghini, B. AlMangour, D. Grzesiak, and M. Pellizzari, Mater. Sci. Eng. A 753, 109–121 https://doi.org/ 10.1016/j.msea.2019.03.027 (2019).
24. C. Lesch, N. Kwiaton, and F.B. Klose, Steel Res. Int. 88, 1– 21 https://doi.org/10.1002/srin.201700210 (2017).
25. D. Raabe, et al. Metall. Mater. Trans. A Phys. Metall. Mater. Sci. 51, 5517–5586, https://doi.org/10.1007/s11661-020-0594 7-2 (2020).
26. J. Zhao, and Z. Jiang, Prog. Mater. Sci. 94, 174–242 https://d oi.org/10.1016/j.pmatsci.2018.01.006 (2018).
27. B.C. De Cooman, Y. Estrin, and S.K. Kim, Twinning-induced plasticity (TWIP) steels. Acta Mater. 142, 283–362 h ttps://doi.org/10.1016/j.actamat.2017.06.046 (2018).
28. W. Zhang, and J. Xu, Mater. Des. 221, 110994 https://doi. org/10.1016/j.matdes.2022.110994 (2022).
29. S. Khaple, B.R. Golla, and V.V.S. Prasad, Def. Technol. 26, 1–22 https://doi.org/10.1016/j.dt.2022.11.019 (2023).
30. S. Singh, and T. Nanda, IJSRD-Int. J. Sci. Res. Dev. 2, 2321–613 (2014).
31. R. Rana, Mater. Sci. Technol. 35, 2039–2044 https://doi.org/10.1080/02670836.2019.1673971 (2019).
32. M. Franceschi, G. Stornelli, R. Perrone, L. Pezzato, A. Di Schino, and M. Dabala`, Steel Res. Int.
33. D.K. Matlock and J.G. Speer, 3rd Int. Conf. Adv. Struct. Steels 774–781 (2006).
34. T. Nanda, V. Singh, V. Singh, A. Chakraborty, and S. Sharma, Proc. Inst. Mech. Eng. Part L J. Mater. Des. Appl. 233, 209–238 https://doi.org/10.1177/1464420716664198 (2019).
35. H.K.D.H. Bhadeshia, and D.V. Edmonds, Acta Metall. 28, 1265–1273 https://doi.org/10.1016/0001-6160(80)90082-6 (1980).
36. C. Garcı´a-Mateo, F.G. Caballero, and H.K.D.H. Bhadeshia, Mater. Sci. Forum 500, 495–502 https://doi.org/10.4028/ww w.scientific.net/msf.500-501.495 (2005).
37. C. Garcia-Mateo, F.G. Caballero, and H.K.D.H. Bhadeshia, J. Phys. IV Fr. 112, 255–288 https://doi.org/10.1051/jp4 (2003).
38. C. Garcia-Mateo, T. Sourmail, F.G. Caballero, V. Smanio, M. Kuntz, C. Ziegler, A. Leiro, E. Vuorinen, R. Elvira, and T. Teeri, Mater. Sci. Technol. 30, 1071–1078 https://doi.org/10. 1179/1743284713Y.0000000428 (2014).
39. L. Morales-Rivas, C. Garcia-Mateo, T. Sourmail, M. Kuntz, R. Rementeria, and F.G. Caballero, Metals. https://doi.org/ 10.3390/met6120302 (2016).
40. H.K.D.H. Bhadeshia, Bainite in steels: theory and practice; maney publishing, vol. 19; ISBN 9781909662742 (2006).
41. M. Franceschi, C. Soffritti, A. Fortini, L. Pezzato, G.L. Garagnani, and M. Dabala`, Tribol. Int. https://doi.org/10.1 016/j.triboint.2022.108071 (2023).
42. M. Franceschi, A. Miotti Bettanini, L. Pezzato, M. Dabala`, and P.J. Jacques. Metals. https://doi.org/10.3390/met11122 055 (2021).
43. M. Franceschi, R. Bertolini, A. Fabrizi, M. Dabala`, and L. Pezzato, Mater. Sci. Eng. A. https://doi.org/10.1016/j.msea. 2022.144553 (2023).
44. A. Kro´licka, A.M. Zak, and F.G. Caballero,− Mater. Des. h ttps://doi.org/10.1016/j.matdes.2021.110143 (2021).
45. K.S. Kim, Y.K. Kim, and K.A. Lee, Addit. Manuf. 60, 103262 https://doi.org/10.1016/j.addma.2022.103262 (2022).
46. M. Franceschi, A. Yazdanpanah, D. Leone, L. Pezzato, and M. Dabala`, Metals. https://doi.org/10.3390/met14010113 (2024).
47. A. Kro´licka, and J. Malawska, Materials. https://doi.org/10. 3390/ma17194699 (2024).

48. L. Caprio, A.G. Demir, G. Chiari, and B. Previtali, J. Phys. Photonics. https://doi.org/10.1088/2515-7647/ab7080 (2020).
49. M. Franceschi, L. Morales-Rivas, E. Cordova-Tapia, J.A. Jimenez, M. Dabala`, and C. Garcia-Mateo, J. Mater. Res. Technol. 32, 2931–2944 https://doi.org/10.1016/j.jmrt.2024. 08.141 (2024).
50. M. Franceschi, L. Pezzato, C. Gennari, D. Hanoz, R. Bertolini, A. Fabrizi, M. Polyakova, K. Brunelli, F. Bonollo, and M. Dabala`, Influence of Austempering temperature on microstructure and mechanical properties of high silicon carbide free Bainitic steel. Steel Res. Int. (2023).
51. Corporation, O. Origin(Pro) (2022).
52. L. Lutterotti, Acta Crystallogr. Sect. A Found. Crystallogr. 56, s54–s54 https://doi.org/10.1107/s0108767300021954 (2000).
53. N. Ahmed, I. Barsoum, G. Haidemenopoulos, and R.K.A. AlRub, J. Manuf. Process. 75, 415–434 https://doi.org/10.1016/ j.jmapro.2021.12.064 (2022).
54. K. Sun, W. Peng, L. Yang, and L. Fang, Metals. https://doi. org/10.3390/met10020292 (2020).
55. U. Scipioni Bertoli, G. Guss, S. Wu, M.J. Matthews, and J.M. Schoenung, Mater. Des. 135, 385–396 https://doi.org/ 10.1016/j.matdes.2017.09.044 (2017).
56. Q. Shi, D. Gu, M. Xia, S. Cao, and T. Rong, Opt. Laser Technol. 84, 9–22 https://doi.org/10.1016/j.optlastec.2016.04. 009 (2016).
57. J. Platl, S. Bodner, C. Hofer, A. Landefeld, H. Leitner, C. Turk, M.A. Nielsen, A.G. Demir, B. Previtali, J. Keckes, et al., Acta Mater. 225, 117570 https://doi.org/10.1016/j.acta mat.2021.117570 (2022).
58. C. Garcı´a de Andre´s, F.G. Caballero, C. Capdevila, and L.F. A´lvarez, Mater. Charact. 48, 101–111 https://doi.org/10.101 6/S1044-5803(02)00259-0 (2002).
59. C. Chen, S. Chang, J. Zhu, Z. Xiao, H. Zhu, and X. Zeng, J. Manuf. Process. 59, 621–628 https://doi.org/10.1016/j.jmapr o.2020.10.009 (2020).
60. M. Franceschi, L. Pezzato, C. Gennari, A. Fabrizi, M. Polyakova, D. Konstantinov, K. Brunelli, M. Dabala`, and M. Dabal, Metals 10, 1–19 https://doi.org/10.3390/met10111448 (2020).
61. D. Kotzem, T. Arold, T. Niendorf, and F. Walther, Mater. Sci. Eng. A 772, 138785 https://doi.org/10.1016/j.msea.2019. 138785 (2020).
62. Z.C. Oter, Y. Gencer, and M. Tarakci, Optik (Stuttg) 202, 163568 https://doi.org/10.1016/j.ijleo.2019.163568 (2020).
63. B. Ferrar, L. Mullen, E. Jones, R. Stamp, and C.J. Sutcliffe, J. Mater. Process. Technol. 212, 355–364 https://doi.org/10. 1016/j.jmatprotec.2011.09.020 (2012).
64. Z. Chen, X. Wu, D. Tomus, and C.H.J. Davies, Addit. Manuf. 21, 91–103 https://doi.org/10.1016/j.addma.2018.02.009 (2018).
65. T.P. Moran, D.H. Warner, A. Soltani-Tehrani, N. Shamsaei, and N. Phan, Addit. Manuf. 47, 102333 https://doi.org/10. 1016/j.addma.2021.102333 (2021).
66. J. Boes, A. Ro¨ttger, C. Mutke, C. Escher, and W. Theisen, Addit. Manuf. 23, 170–180 https://doi.org/10.1016/j.addma. 2018.08.005 (2018).
67. K. Kempen, B. Vrancken, S. Buls, L. Thijs, J. Van Humbeeck, and J.P. Kruth, J. Manuf. Sci. Eng. 136, 1–7 https://d oi.org/10.1115/1.4028513 (2014).
68. L. Zhou, J. Sun, J. Chen, W. Chen, Y. Ren, Y. Niu, C. Li, and W. Qiu, J. Alloys Compd. 928, 167130 https://doi.org/10.10 16/j.jallcom.2022.167130 (2022).
69. J.H. Park, G.B. Bang, K.A. Lee, Y. Son, Y.H. Song, B.S. Lee, W.R. Kim, and H.G. Kim, Met. Mater. Int. 28, 2836–2848 h ttps://doi.org/10.1007/s12540-022-01169-w (2022).
70. L. Cordova, T. Bor, M. de Smit, M. Campos, and T. Tinga, Addit. Manuf. 32, 101082 https://doi.org/10.1016/j.addma.2 020.101082 (2020).
71. L. Cheng, A. Bottger, T.H. de Keijser, and E.J. Mittemeijer, Scr. Metall. Mater. 24, 509–514 (1990).
72. R. Rementeria, J.D. Poplawsky, M.M. Aranda, W. Guo, J.A. Jimenez, C. Garcia-Mateo, and F.G. Caballero, Acta Mater. 125, 359–368 https://doi.org/10.1016/j.actamat.2016.12.013 (2017).